Supplementary Information (SI) for CrystEngComm.
This journal is © The Royal Society of Chemistry 2025

Supplementary Information

B-Site Substitution in A_2BO_4 Ruddlesden-Popper Perovskites for Enhanced OER and HER in Alkaline Medium.

Yuhu Huang[1,2], Jin Li[1,2], Yuda Yu[1,2], Jiaping Hu[1,2], Han-Shu Xu[3] and Kaibin Tang[1,2]*

[1] Hefei National Research Center for Physical Sciences at the Microscale, University of Science and Technology of China, Hefei, 230026, China.
[2] Department of Chemistry, University of Science and Technology of China, Hefei, 230026, China.
[3] Department of Applied Physics, School of Biomedical Engineering, Anhui Medical University, Hefei, 230032, China.

1.1 Synthesis of the catalysts

The all catalysts were synthesized using a modified Pechini method. Taking the synthesis of $PrSrCo_{0.6}Fe_{0.4}O_4$ as a representative example: 1 mmol of $Pr(NO_3)_3 \cdot 6H_2O$ (AR, SCRC), 1 mmol $Sr(NO_3)_2$ (AR, SCRC), 0.6 mmol $Co(NO_3)_2 \cdot 6H_2O$ (AR, SCRC) and 0.4 mmol $Fe(NO_3)_2 \cdot 9H_2O$ (AR, SCRC) were dissolved in 50 ml deionized water. Subsequently, 4.5 mmol of citric acid (CA) (analytical reagent, SCRC) and 3 mmol of ethylenediamineteraacetic acid (EDTA, AR, SCRC) was added as complexing agents to promote uniform dispersion of the metal ions. The pH value was then adjusted to 7-8 by the addition of $NH_3 \cdot H_2O$ (25%, SCRC). The resulting solution underwent spontaneous combustion upon heating in an evaporating dish, resulting in a black ash. This ash was thoroughly ground using a mortar and subsequently transferred to an Al_2O_3 crucible, where it was subjected to calcination in a muffle furnace at 1150℃ for 10 hours to obtain the desired $PrSrCo_{0.6}Fe_{0.4}O_4$ product. For the synthesis of $PrSrCo_{0.6}Fe_{0.4-z}Ni_zO_4$, $Ni(NO_3)_2 \cdot 6H_2O$ (AR, SCRC) was used to partially replace $Fe(NO_3)_2 \cdot 9H_2O$ in appropriate proportions, while keeping the total molar amount of Fe and Ni constant at 0.4 mmol. In the case of noble-metal substitution (Ir or Ru), the $PrSrCo_{0.6}Fe_{0.4-x}M_xO_4$ (M = Ir, Ru) catalysts were synthesized by substituting a portion of the $Fe(NO_3)_2 \cdot 9H_2O$ with pre-dissolved $IrCl_4 \cdot nH_2O$ or $RuCl_3 \cdot nH_2O$. The remaining synthesis steps were consistent with those used for $PrSrCo_{0.6}Fe_{0.4}O_4$.

1.2 Characterization

The synthesized compounds underwent characterization through X-ray diffraction (XRD) analysis conducted using a Rigaku SmartLab SE diffractometer, utilizing Cu Kα radiation (λ = 1.5418 Å) at 40 KV and 40 mA. XRD patterns were collected at room temperature within the 2θ range of 10-80°, with an interval of 0.02°. Detailed structural information was then refined using the Rietveld method within the GSAS-II software. Comprehensive evaluations of morphology and composition were conducted utilizing a range of techniques. Scanning electron microscopy (SEM) was performed employing a JEOLJSM-6700F instrument. X-ray photoelectron spectroscopy (XPS) investigations were carried out using an ESCALAB250Xi spectroscope. And the field emission high-resolution transmission electron microscopy (HRTEM) equipped with energy-dispersive X-ray spectroscopy (EDX) was employed, utilizing a Talos F200X instrument. Additionally, specific surface areas were determined utilizing the Brunauer-Emmett-Teller (BET) technique, employing a Micromeritics ASAP 2460 instrument. Furthermore, magnetization characteristics were assessed using a SQUID magnetometer (MPMS3, Quantum Design).

1.3 Electrochemical Measurements

The electrochemical performance of the catalyst was assessed using a standard three-electrode system in a 1M KOH electrolyte at room temperature, employing the CHI760E electrochemical workstation. To prepare the working electrode, 5 mg of the catalyst and 1 mg of conductive carbon black were dispersed in 800 μL of ethanol. Subsequently, 40 μL of Nafion was added, and the resulting mixture underwent ultrasonication for approximately 1 hour to achieve a homogeneous ink. A 5 μL aliquot of the ink was then deposited onto a glassy carbon electrode (diameter = 3 mm) and dried at room temperature, resulting in a catalyst loading of 0.421 mg cm^{-2}. The Pt wire and 1M

KOH Hg/HgO were employed as the counter electrode and reference electrode, respectively.

The perovskite electrocatalysts underwent activation through 20 cycles of cyclic voltammetry (CV) scans conducted between 0.1-0.9 V vs. Hg/HgO at a scan rate of 100 mV s^{-1}. Following activation, polarization curves were generated using linear sweep voltammetry (LSV) at a scan rate of 5 mV s^{-1}. These polarization curves were then reanalyzed by plotting overpotential (η) against the logarithm of current density (log |j|) to derive Tafel plots. The linear segments of the Tafel plots were subsequently fitted to the Tafel equation ($\eta = b \log |j| + a$) to determine the Tafel slope. Furthermore, electrochemical impedance spectroscopy (EIS) was conducted at 1.57 V vs. RHE over a frequency range spanning 100 kHz to 0.1 Hz, applying an AC voltage of 5 mV. The electrochemical double-layer capacitance (C_{dl}) was obtained from CV results recorded between 0.1 V and 0.2 V vs. Hg/HgO at scan rates of 20, 40, 60, 80, 100, 120, 140, and 160 mV s^{-1}. The calculation of mass activity (MA, A g^{-1}) is determined using the following equation:

$$MA = |J|/m \tag{1-1}$$

where, J represents the current density (mA cm^{-2}), and m is the mass loading of the catalyst, approximately 0.425 mg cm^{-2}.

The turnover frequency (TOF) for all the catalysts has been calculated using the following relation:

$$TOF = |J|/(nFC) \tag{1-2}$$

where, the symbols represent the following parameters:

J: Measured current density value (mA cm^{-2}) at a specific overpotential.

C: The density of catalytically active metal sites (mol cm^{-2}).

n: Number of electron transfers, where n = 4 for OER and n = 2 for HER.

F: Faraday constant, with a numerical value of 96,485 C mol^{-1}.

For HER measurements, the counter electrode was replaced with a graphite rod, and the tests were conducted within a potential range of -0.9 to -1.5 V vs. Hg/HgO. EIS was performed at -0.32 V vs. RHE, while the C_{dl} was measured in the potential window of -0.7 to -0.8 V vs. Hg/HgO. All other testing procedures were consistent with those used for OER measurements.

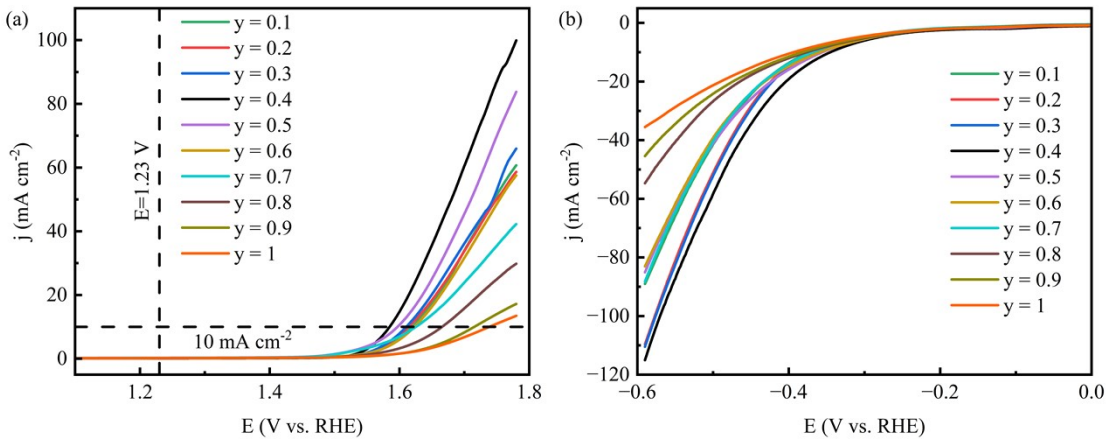

Fig. S1 Electrocatalytic performance of $PrSrCo_{1-y}Fe_yO_4$: (a) LSV curves for OER; (b) LSV curves for HER.

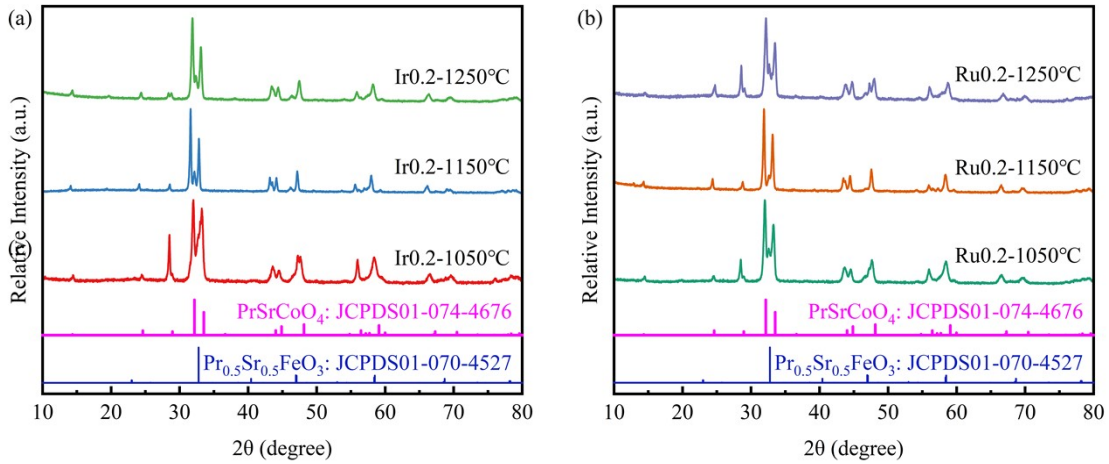

Fig. S2 XRD patterns of (a) $PrSrCo_{0.6}Fe_{0.2}Ir_{0.2}O_4$ and (b) $PrSrCo_{0.6}Fe_{0.2}Ru_{0.2}O_4$ at different calcination temperatures.

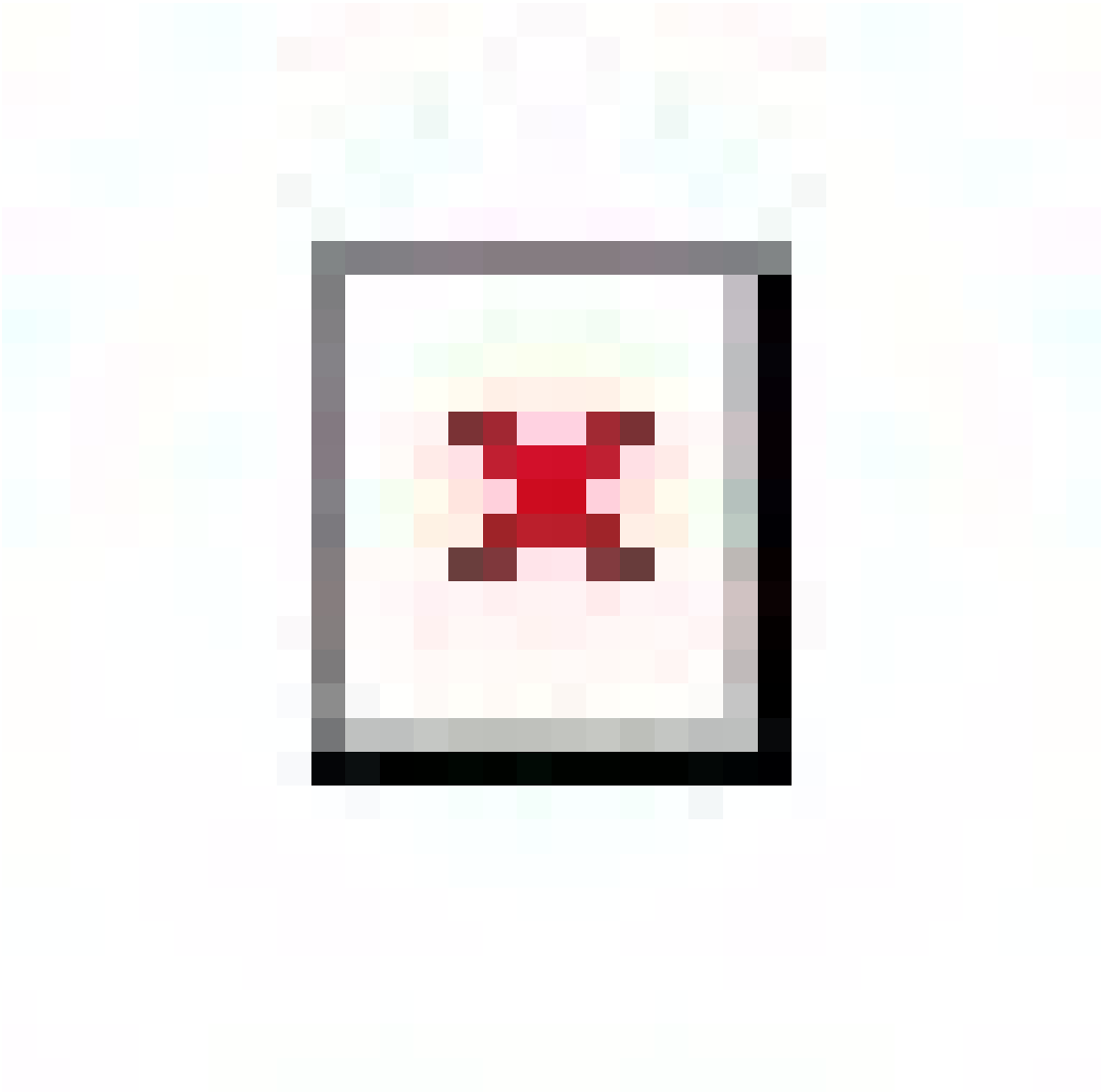

Fig. S3 (a-c) XRD patterns of Ir0.1 catalysts at different calcination temperatures, (d) XRD patterns of Ir0.1 catalysts with different calcination times, and corresponding (e) OER and (f) HER. The LSV data for Ir0.1 (1150℃-10h) used here are reproduced from Fig. 4a and Fig. 5a.

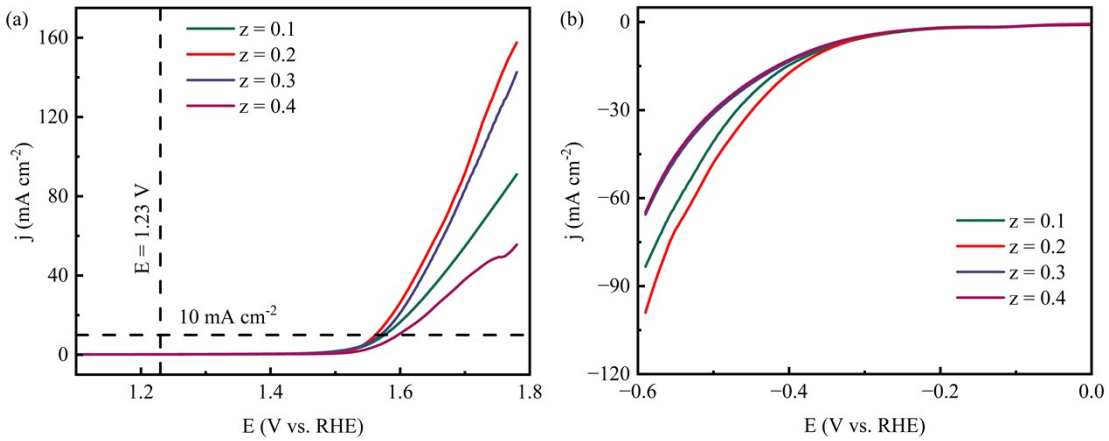

Fig. S4. Electrocatalytic performance of $PrSrCo_{0.6}Fe_{0.4-z}Ni_zO_4$: (a) LSV curves for OER; (b) LSV curves for HER.

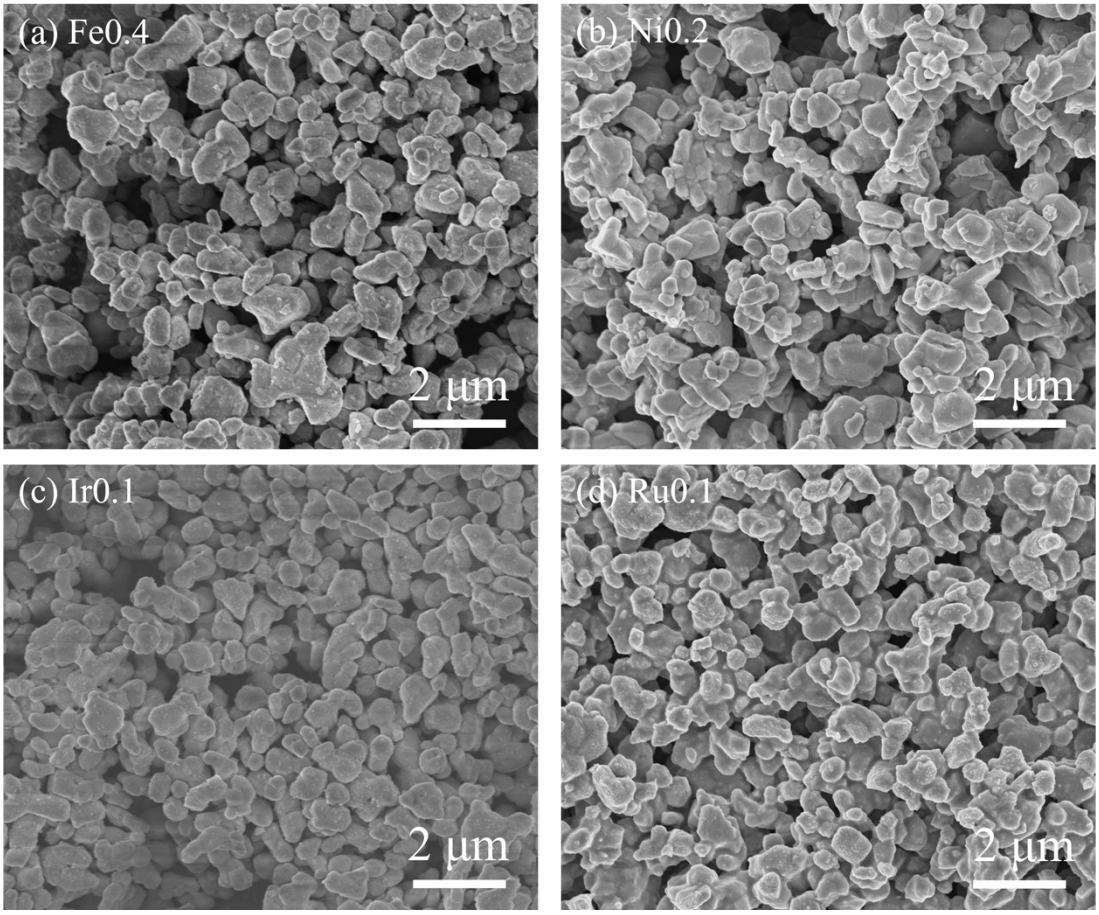

Fig. S5 SEM images of (a) Fe0.4, (b) Ni0.2, (c) Ir0.1 and (d) Ru0.1.

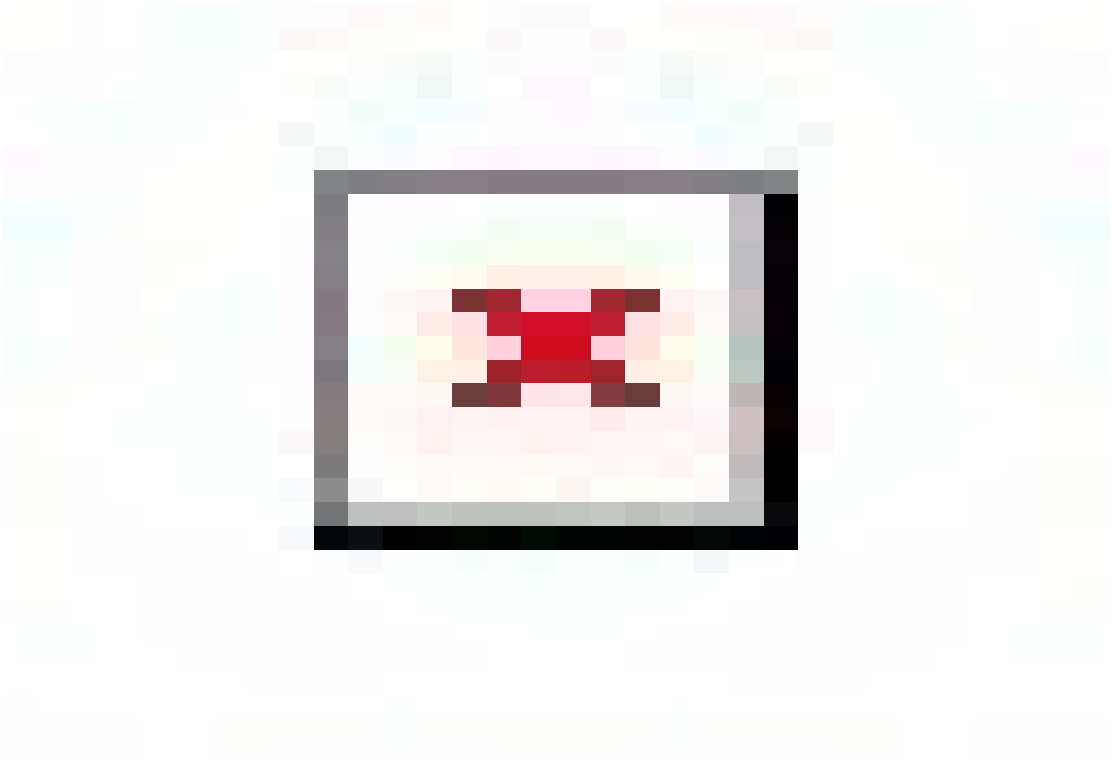

Fig. S6 The N_2 adsorption-desorption isotherms (a) and the corresponding BJH pore size distribution plots (b) in Fe0.4, Ni0.2, Ir0.1 and Ru0.1.

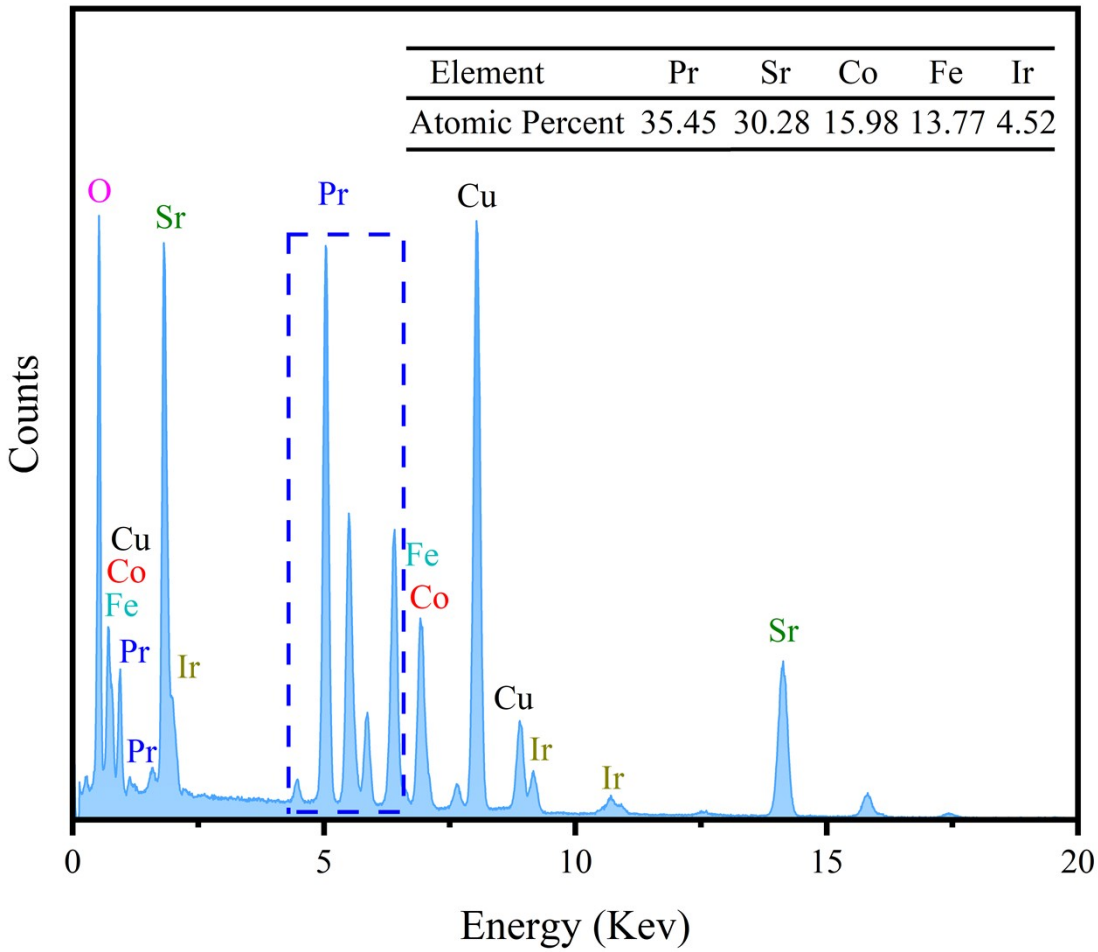

Fig. S7 EDX spectrum of Ir0.1.

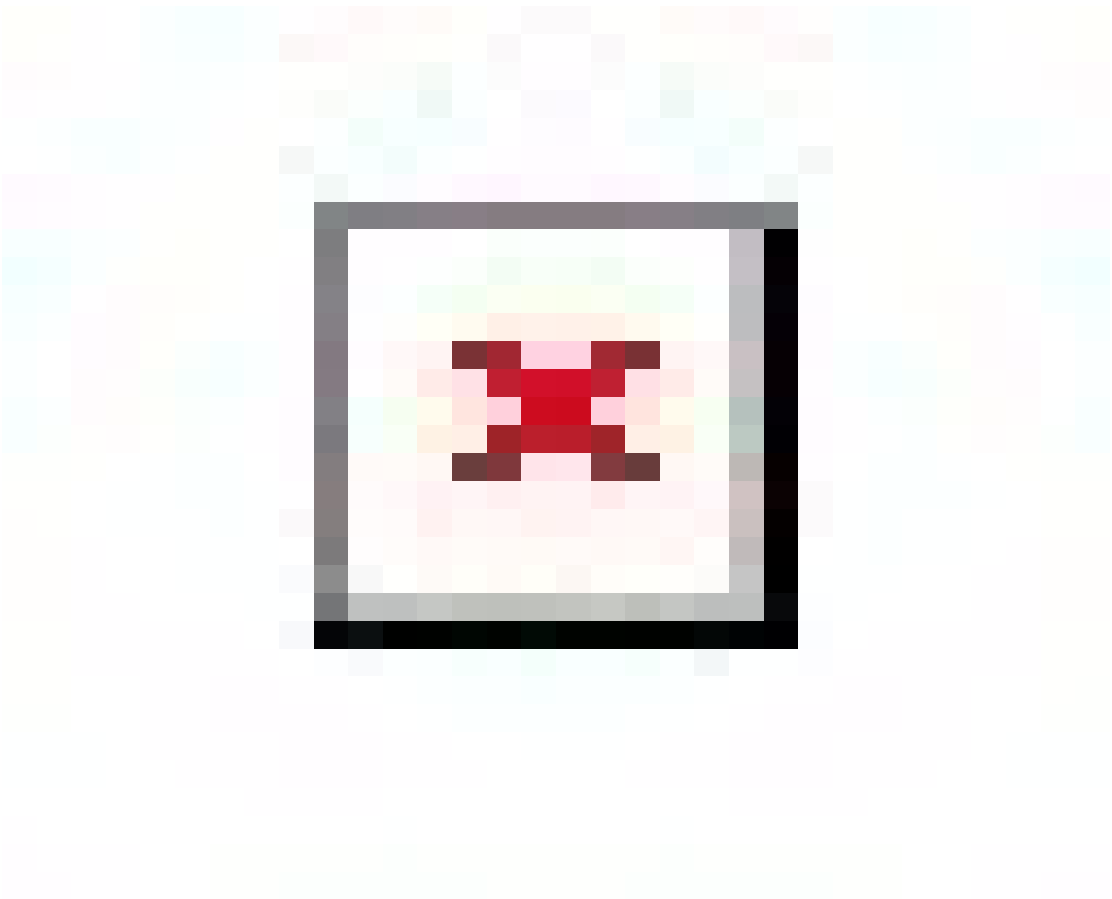

Fig. S8 CV curves of Fe0.4, Ni0.2, Ir0.1 and Ru0.1 under OER test at scan rates of 20, 40, 60, 80, 100, 120, 140, 160 mV s^{-1} under 0.1−0.2 V vs. Hg/HgO.

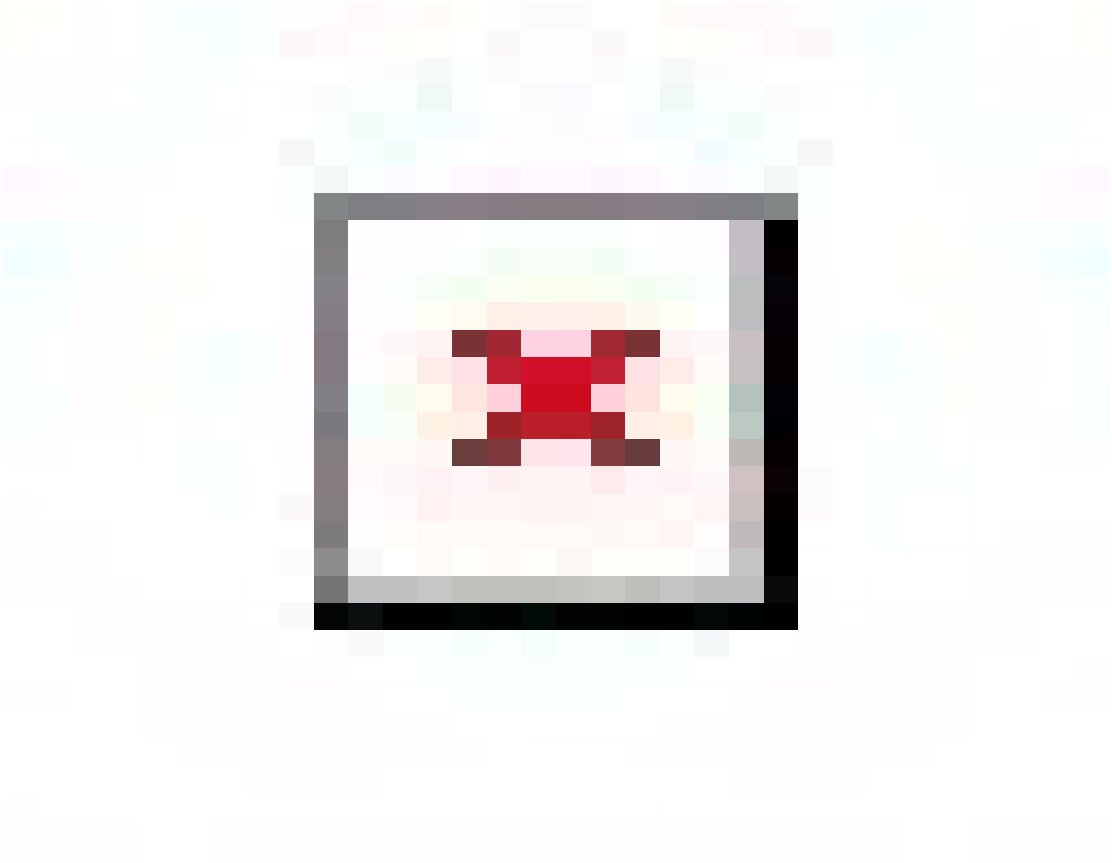

Fig. S9 (a) MA, (b) TOF, (c) Chronopotentiometry test of Fe0.4, Ni0.2, Ir0.1 and Ru0.1 under OER test at 10 mA cm^{-2}.

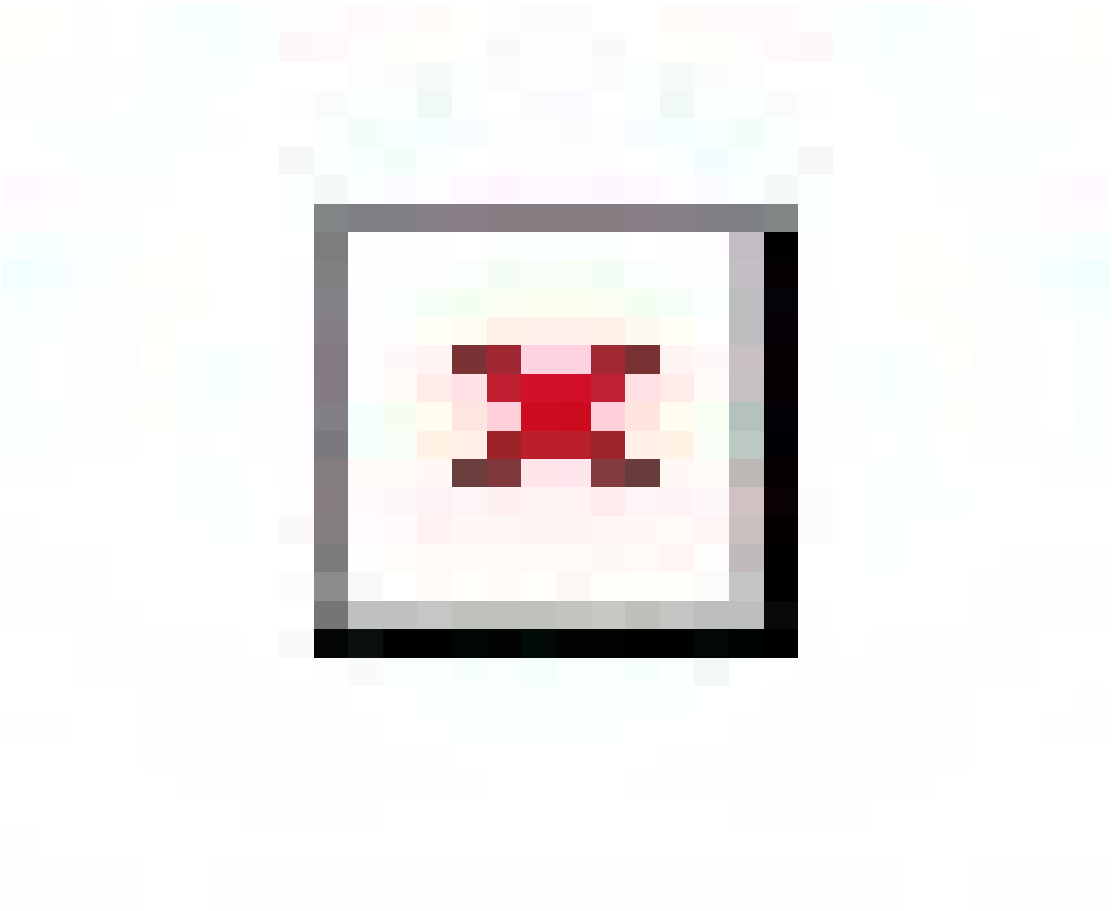

Fig. S10 CV curves of Fe0.4, Ni0.2, Ir0.1 and Ru0.1 under HER test at scan rates of 20, 40, 60, 80, 100, 120, 140, 160 mV s^{-1} under -0.7−-0.8 V vs. Hg/HgO.

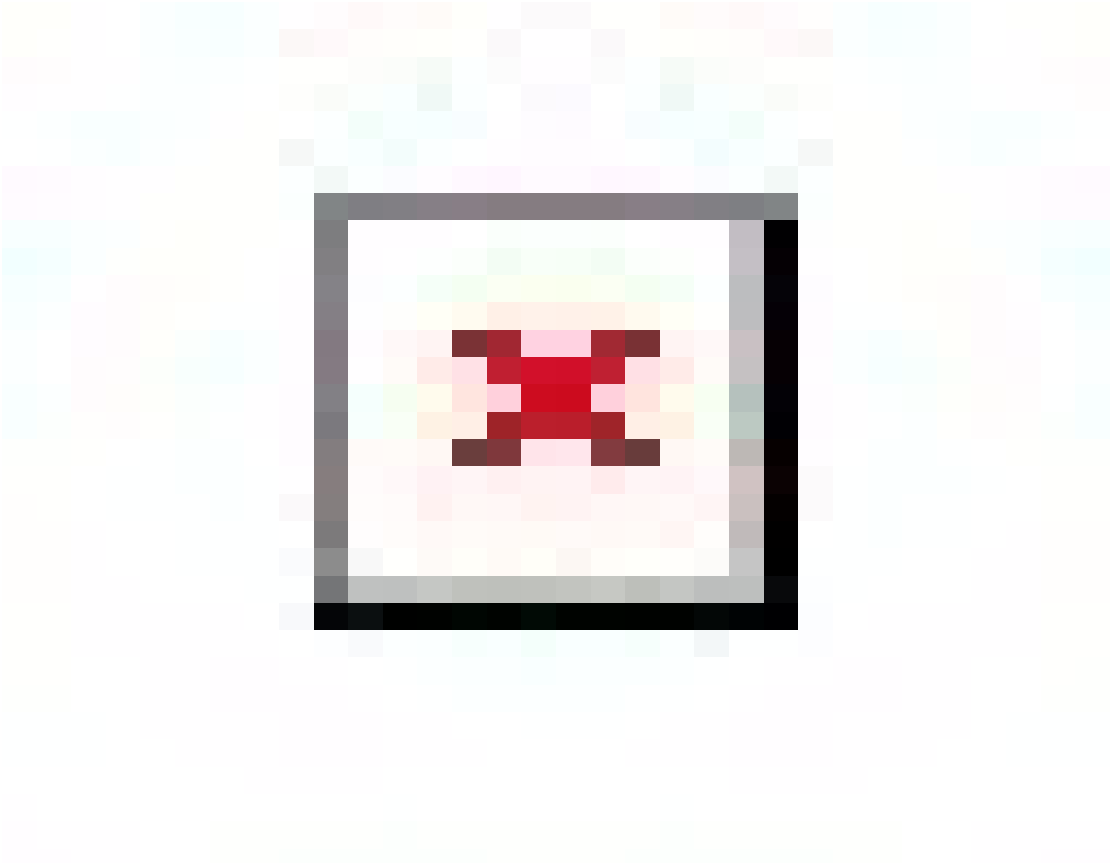

Fig. S11 (a) MA, (b) TOF, (c) Chronopotentiometry test of Fe0.4, Ni0.2, Ir0.1 and Ru0.1 under HER test at 10 mA cm^{-2}.

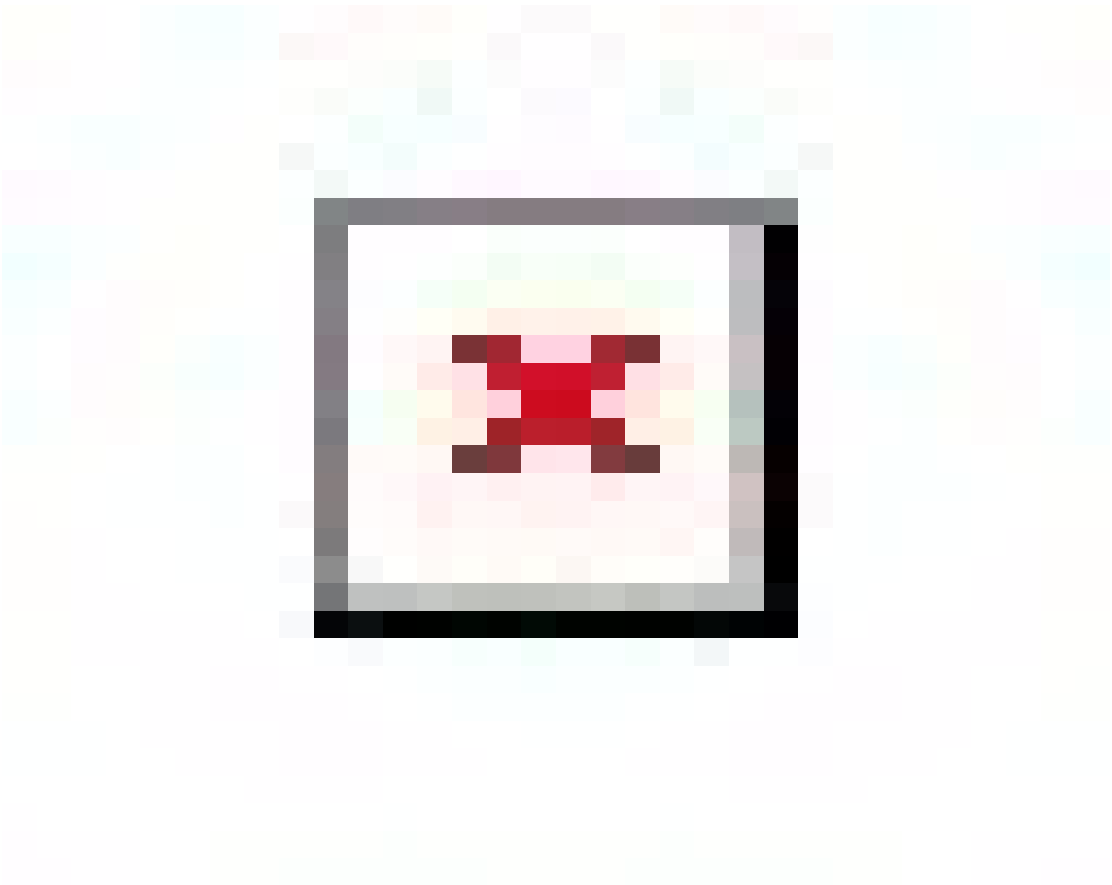

Fig. S12 (a), (c) OER and HER polarization curves normalized by geometric area; (b), (d) The corresponding curves normalized by ECSA. The LSV data for Fe0.4, Ni0.2, Ir0.1 and Ru0.1 used here are reproduced from Fig. 4a and Fig. 5a.

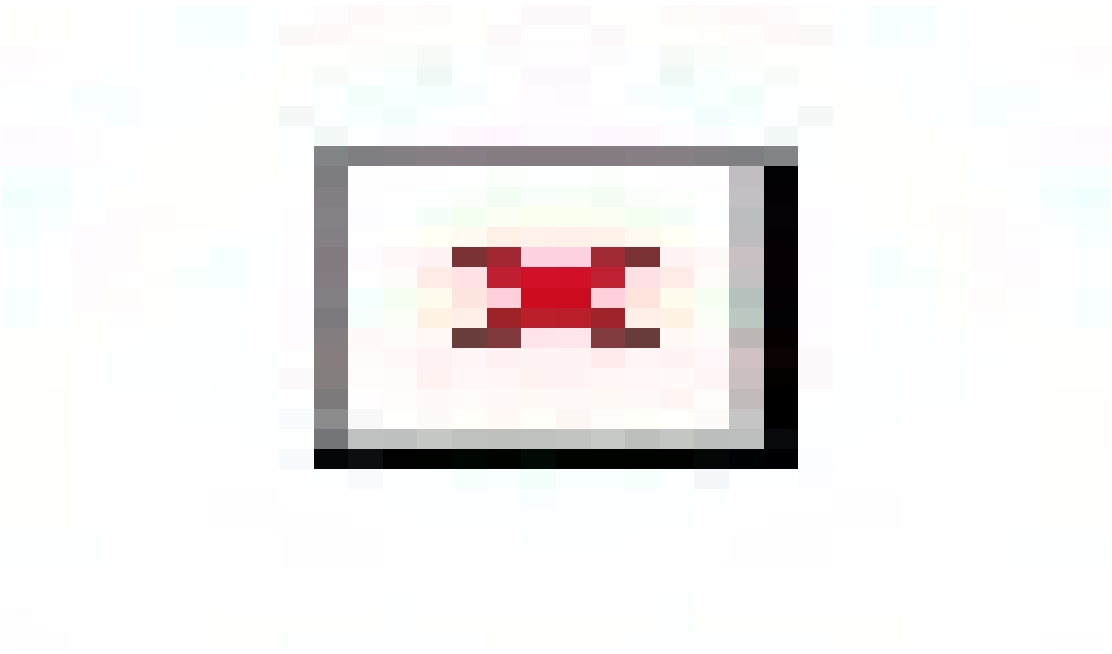

Fig. S13 XPS spectra of (a) Full spectral, (b) Fe 2p, (c) Ni 2p in Ni0.2, (d) Ir 4f in Ir0.1, and (e) Ru 3p in Ru0.1.

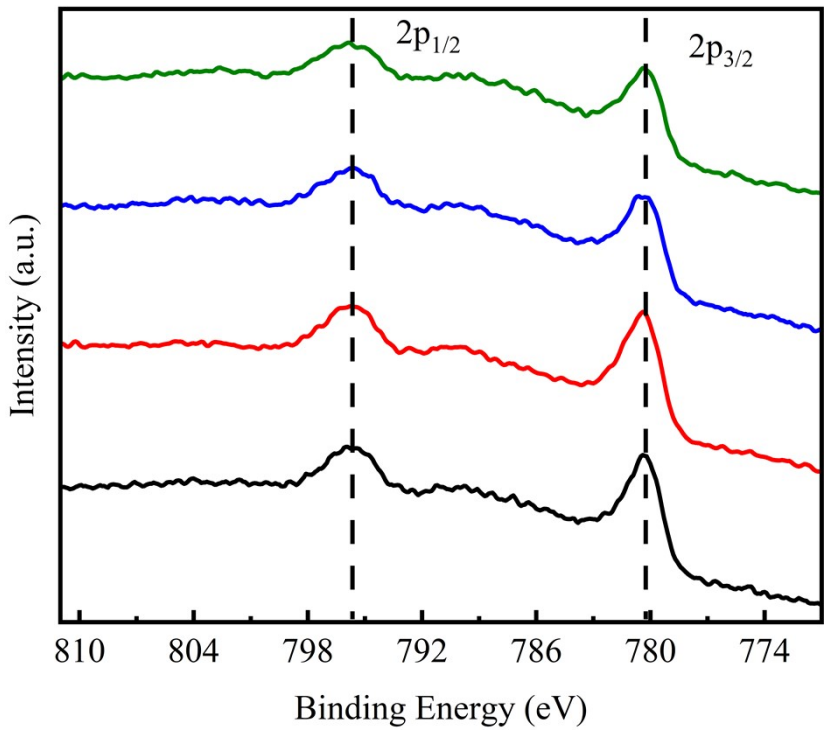

Fig. S14 XPS spectra of Co 2p.

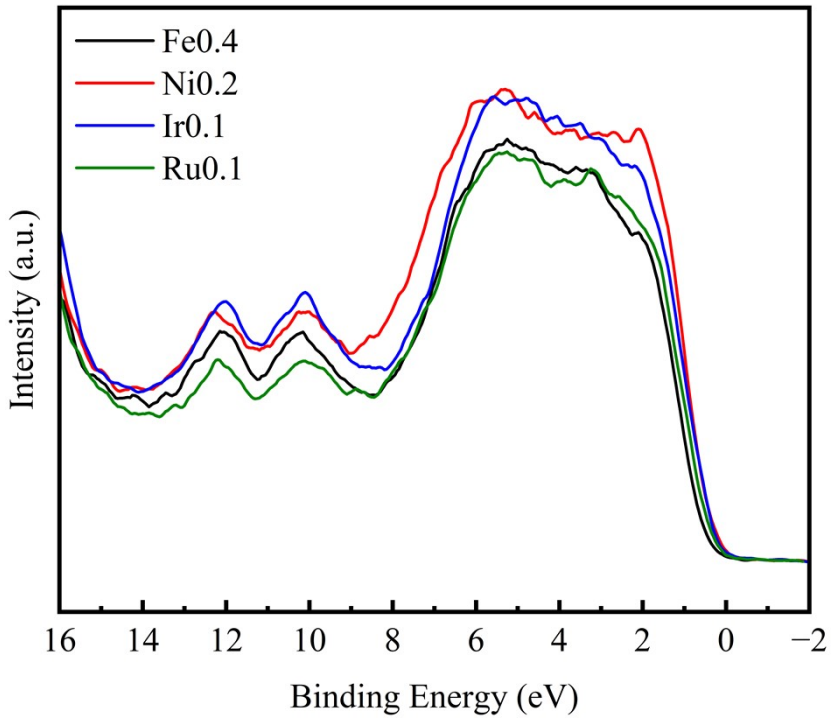

Fig. S15 valance-band spectra of Fe0.4, Ni0.2, Ir0.1 and Ru0.1.

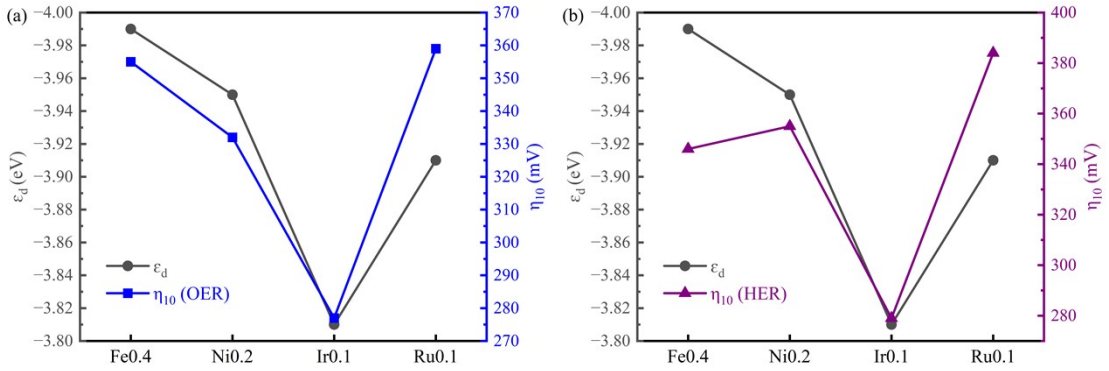

Fig. S16 Relationship between ε_d and electrocatalytic activity: (a) OER; (b) HER.

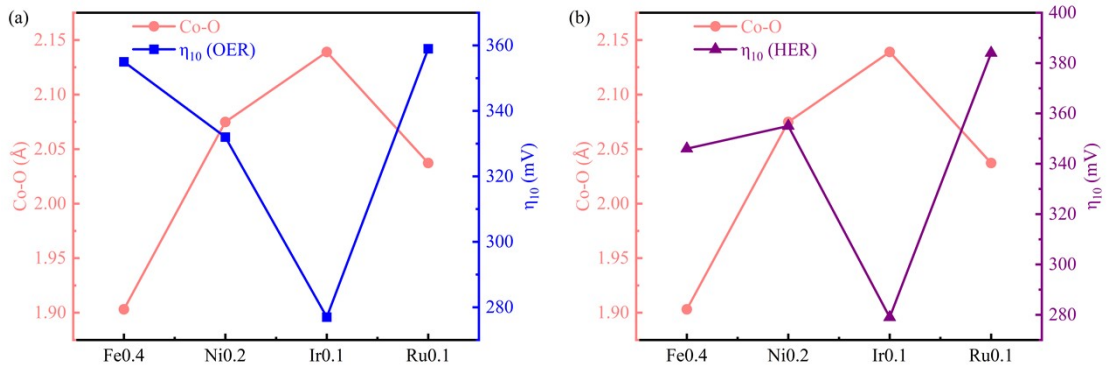

Fig. S17 Relationship between Co-O bond length and electrocatalytic activity: (a) OER; (b) HER.

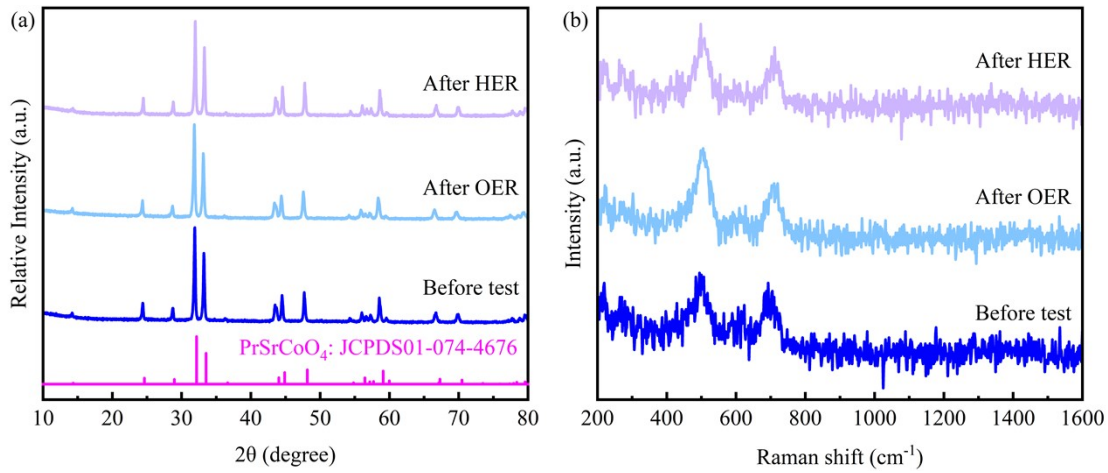

Fig. S18 (a) XRD and (b) Raman results of Ir0.1 before the electrochemical reaction and after long-term stability tests.

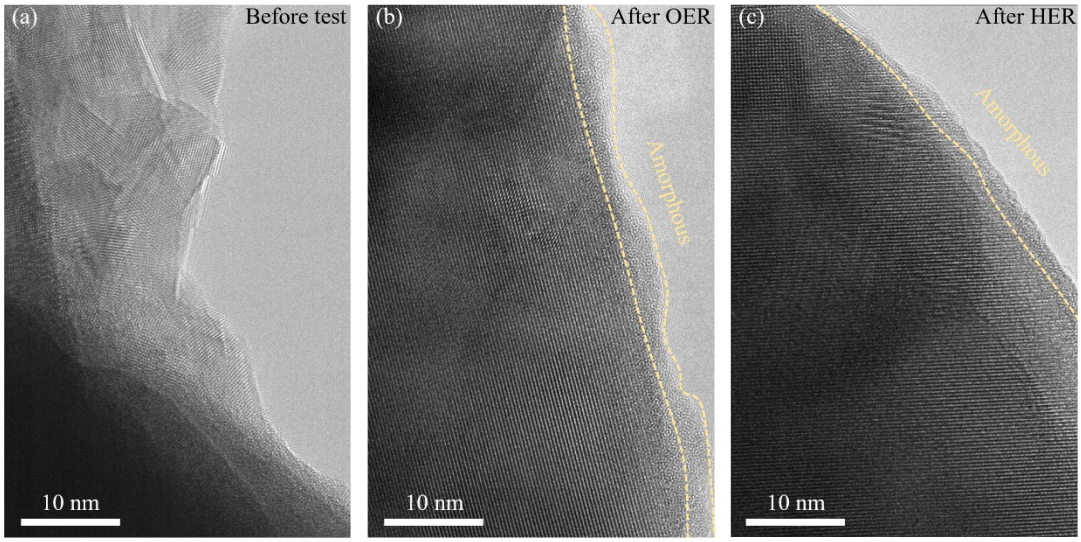

Fig. S19 HRTEM images of the Ir0.1 catalyst: (a) pristine sample before electrocatalysis, and after long-term stability tests for (b) OER and (c) HER.

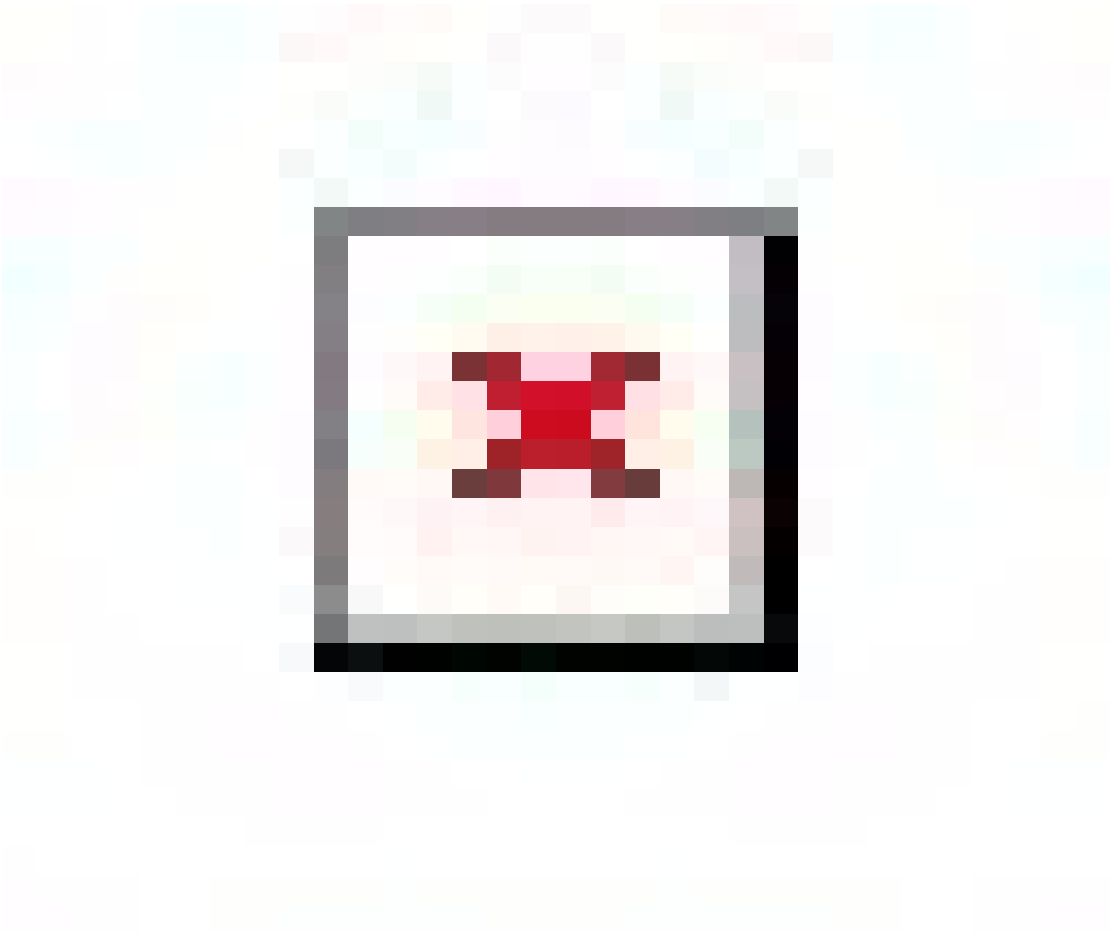

Fig. S20 XPS results of Ir0.1 before the electrochemical reaction and after long-term stability tests. (a) Co 2p, (b) Fe 2p, (c) Ir 4f and (d) O 1s.

Table S1. Lattice parameters and reliability factors from Rietveld refinements.

	Fe0.4	Ni0.2	Ir0.1	Ru0.1
Space group	*I4/mmm*	*I4/mmm*	*I4/mmm*	*I4/mmm*
a/b/Å	3.80468	3.79543	3.81633	3.80197
c/Å	12.41263	12.41820	12.40114	12.39066
V/Å^3	179.680	178.887	180.615	179.107
α/β/γ (deg)			α=β=γ=90°	
R_p (%)	3.17	3.42	3.32	3.66
R_{wp} (%)	4.76	5.07	4.72	4.97
χ^2 (%)	3.87	4.40	3.65	2.63

Table S2. Summary of recently reported perovskite oxide electrocatalysts for OER. η_{10} represent the overpotential at 10 mA cm^{-2}.

Catalyst	Electrolyte	η_{10} (mV)	Reference
Sr_2IrO_4 modified $SrIrO_3$	0.1 M $HClO_4$	245	1
Ir0.1	1 M KOH	277	**Our work**
$SrIrO_3$	1 M KOH	290	2
$PrSr_3Co_{1.5}Fe_{1.5}O_{10-\delta}$	0.1 M KOH	294	3
$SrCo_{0.4}Fe_{0.2}W_{0.4}O_{3-\delta}$	1 M KOH	300	4
$LaFe_xNi_{1-x}O_3$	1 M KOH	302	5
$NdFe_{1-x}Ni_xO_3$	1 M KOH	310	6
$La_{1-x}Pr_xCoO_3$	1 M KOH	312	7
Ni0.2	1 M KOH	332	**Our work**
$Sr_3(Co_{0.8}Fe_{0.1}Nb_{0.1})_2O_{7-\delta}$	0.1 M KOH	334	8
$LaSr_3Co_{1.5}Fe_{1.5}O_{10-\delta}$	0.1 M KOH	341	3
Fe0.4	1 M KOH	355	**Our work**
Ru0.1	1 M KOH	359	**Our work**
$PrBaCo_2O_{5.75}$	1 M KOH	360	9
$PrSrCoO_4$	1 M KOH	375	10
$NdSr_3Co_{1.5}Fe_{1.5}O_{10-\delta}$	0.1 M KOH	375	3
$La_{0.9}CoO_{3-\delta}$	0.1 M KOH	380	11
$La_{0.7}Sr_{0.3}CoO_{3-\delta}$	0.1 M KOH	390	12
$PrBaCo_2O_{5.5}$	1 M KOH	420	9
$Sr_{0.95}Co_{0.8}Nb_{0.1}Ni_{0.1}O_{3-\delta}$	1 M KOH	438	13
$Pr_{0.5}Ba_{0.5}CoO_{3-\delta}$	0.1 M KOH	440	14
$LaCoO_3$	1 M KOH	470	15

Table S3. Summary of recently reported perovskite oxide electrocatalysts for HER. η_{10} represent the overpotential at 10 mA cm^{-2}.

Catalyst	Electrolyte	η_{10} (mV)	Reference
$(Gd_{0.5}La_{0.5})BaCo_2O_{5.5+\delta}$	1 M KOH	210	16
$PrBaCo_2O_{5.8}$	1 M KOH	240	17
$PrBaCo_2O_{5+\delta}$-1100	0.1 M KOH	245	18
$SrNb_{0.1}Co_{0.7}Fe_{0.2}O_{3-\delta}$	0.1 M KOH	262	19
Ir0.1	1 M KOH	279	**Our work**
$NdBaMn_2O_{5.5}$	1 M KOH	290	20
$Sr_{0.95}Nb_{0.1}Co_{0.7}Ni_{0.2}O_{3-\delta}$	1 M KOH	299	21
$La_{0.96}Ce_{0.04}CoO_{3-\delta}$	1 M KOH	305	22
$SrCo_{0.7}Fe_{0.25}Mo_{0.05}O_{3-\delta}$	1 M KOH	323	23
$Ba_{0.5}Sr_{0.5}Co_{0.8}Fe_{0.2}O_{3-\delta}$	1 M KOH	342	24
Fe0.4	1 M KOH	346	**Our work**
Ni0.2	1 M KOH	355	**Our work**
$PrSrCoO_4$	1 M KOH	361	10
Ru0.1	1 M KOH	384	**Our work**
$LaFe_{0.8}Co_{0.2}O_{3-\delta}$	1 M KOH	400	25
$La_{0.5}Sr_{0.5}CoO_{3-\delta}$	1 M KOH	420	26
$La_{0.8}Sr_{0.2}Cr_{0.69}Ni_{0.31}O_{3-\delta}$	0.1 M KOH	447	27

Table S4. The peak area of Co^{3+} and Co^{2+} in Co2p XPS

Electrocatalysts	$Co^{3+}2p_{3/2}$ (Area)	$Co^{3+}2p_{1/2}$ (Area)	$Co^{2+}2p_{3/2}$ (Area)	$Co^{2+}2p_{1/2}$ (Area)
Fe0.4	18348.86	9174.43	6816.84	3408.42
Ni0.2	22709.58	11354.79	8580.06	4290.03
Ir0.1	17244.52	8622.26	6401.12	3200.56
Ru0.1	16958.42	8479.21	6173.32	3086.66

Table S5. The relative concentration of different oxygen species in O1s XPS

Electrocatalysts	lattice O^{2-} (%)	O_2^{2-} /O^- (%)	OH^- or O_2 (%)	H_2O (%)
Fe0.4	16.81%	15.12%	60.50%	7.57%
Ni0.2	16.61%	18.05%	60.65%	4.69%
Ir0.1	15.76%	20.60%	58.27%	5.37%
Ru0.1	18.14%	14.73%	61.57%	5.56%

Table S6. Weiss temperature (θ) and effective magnetic moment (μ_{eff})

	Fe0.4	Ni0.2	Ir0.1	Ru0.1
θ/K	-103.64	-88.75	-109.04	-85.46
μ_{eff}/μ_B	5.03	4.98	5.20	5.17
μ_{eff} (Co)/μ_B	3.15	3.66	3.93	3.78

References

[1] Zhang, L.; Jang, H.; Li, Z.; Liu, H.; Kim, M. G.; Liu, X.; Cho, J. $SrIrO_3$ modified with laminar Sr_2IrO_4 as a robust bifunctional electrocatalyst for overall water splitting in acidic media. *Chem. Eng. J.* **2021**, *419*, 129604.

[2] Shin, S.; Kwon, T.; Kim, K.; Kim, M.; Kim, M. H.; Lee, Y. Single-Phase Perovskite $SrIrO_3$ Nanofibers as a Highly Efficient Electrocatalyst for a pH-Universal Oxygen Evolution Reaction. *ACS Appl. Energy Mater.* **2022**, *5* (5), 6146-6154.

[3] W. Zhu, J. Chen, D. Liu, G. Yang, W. Zhou, R. Ran, J. Yu, Z. Shao. Engineering the oxygen-evolution activity by changing the A-site rare-earth element in $RSr_3Fe_{1.5}Co_{1.5}O_{10-\delta}$ (R=La, Nd, Pr) Ruddlesden-Popper perovskites. *Mater. Chem. Front.* **2023**,7, 4526-4534.

[4] G. Chen, Z. Hu, Y. Zhu, Z.-G. Chen, Y. Zhong, H.-J. Lin, C.-T. Chen, L. H. Tjeng, W. Zhou, Z. Shao. Ultrahigh-performance tungsten-doped perovskites for the oxygen evolution reaction. *J. Mater. Chem. A* **2018**, 6, 9854-9859.

[5] Wang, H.; Wang, J.; Pi, Y.; Shao, Q.; Tan, Y.; Huang, X. Double Perovskite $LaFe_xNi_{1-x}O_3$ Nanorods Enable Efficient Oxygen Evolution Electrocatalysis. *Angew. Chem. Int. Ed.* **2019**, *58* (8), 2316-2320.

[6] Khreif, Y.; Omari, M.; Makhloufi, S. Synthesis and catalytic properties of Ni-doped $NdFeO_3$. *Inorg. Chim. Acta* **2024**, *566*.

[7] Xie, R.; Nie, Z.; Hu, X.; Yu, Y.; Aruta, C.; Yang, N. Pr-Doped $LaCoO_3$ toward Stable and Efficient Oxygen Evolution Reaction. *ACS Appl. Energy Mater.* **2021**, *4* (9), 9057-9065.

[8] Y. Zhu, H. A. Tahini, Z. Hu, Y. Yin, Q. Lin, H. Sun, Y. Zhong, Y. Chen, F. Zhang, H.-J. Lin, C.-T. Chen, W. Zhou, X. Zhang, S. C. Smith, Z. Shao, H. Wang. Boosting oxygen evolution reaction by activation of lattice-oxygen sites in layered Ruddlesden-Popper oxide. *EcoMat*. **2020**; 2: e12021.

[9] X. Miao, L. Wu, Y. Lin, X. Yuan, J. Zhao, W. Yan, S. Zhou, L. Shi. The role of oxygen vacancies in water oxidation for perovskite cobalt oxide electrocatalysts: are more better? *Chem. Commun.* **2019**, 55, 1442-1445.

[10] Huang, Y.; Hu, J.; Li, J.; Xie, W.; Xu, H.-S.; Tang, K. Study on Water Splitting of the 214-Type Perovskite Oxides $LnSrCoO_4$ (Ln = La, Pr, Sm, Eu, and Ga). *Langmuir* **2024**, *40* (19), 9965-9974.

[11] H. Wang, X. Chen, D. Huang, M. Zhou, D. Ding, H. Luo. Cation Deficiency Tuning of $LaCoO_3$ Perovskite as Bifunctional Oxygen Electrocatalyst. *ChemCatChem* **2020**, 12, 2768.

[12] X. Wang, Z. Pan, X. Chu, K. Huang, Y. Cong, R. Cao, R. Sarangi, L. Li, G. Li, S. Feng. Atomic-Scale Insights into Surface Lattice Oxygen Activation at the Spinel/Perovskite interface of $Co_3O_4/La_{0.3}Sr_{0.7}CoO_3$. *Angew. Chem. Int. Ed.* **2019**, 58, 11720.

[13] Q. A. Islam, R. Majee, S. Bhattacharyya. Bimetallic nanoparticle decorated perovskite oxide for state-of-the-art trifunctional electrocatalysis. *J. Mater. Chem. A* **2019**,7,19453–19464.

[14] D. He, G. He, H. Jiang, Z. Chen, M. Huang. Enhanced durability and activity of the perovskite electrocatalyst $Pr_{0.5}Ba_{0.5}CoO_{3-\delta}$ by Ca doping for the oxygen evolution reaction at room temperature. *Chem. Commun.* **2017**, 53, 5132.
[15] Y. Tong, Y. Guo, P. Chen, H. Liu, M. Zhang, L. Zhang, W. Yan, W. Chu, C. Wu, Y. Xie. Spin-State Regulation of Perovskite Cobaltite to Realize Enhanced Oxygen Evolution Activity. *Chem* **2017**, 3, 812.
[16] Guan, D., Zhou, J., Huang, Y.-C., Dong, C.-L., Wang, J.-Q., Zhou, W., Shao, Z. Screening highly active perovskites for hydrogen-evolving reaction via unifying ionic electronegativity descriptor. *Nat. Commun.* 2019, 10, 3755.

[17] Togano, H., Asai, K., Oda, S., Ikeno, H. I., Kawaguchi, S., Oka, K., Wada, K., Yagi, S., Yamada, I. Highly active hydrogen evolution catalysis on oxygen-deficient double-perovskite oxide $PrBaCo_2O_{6-\delta}$. *Mater. Chem. Front.* **2020**, 4, 1519-1529.
[18] Sun, Q., Dai, Z., Zhang, Z., Chen, Z., Lin, H., Gao, Y., Chen, D. Double perovskite PrBaCo2O5.5: An efficient and stable electrocatalyst for hydrogen evolution reaction. *J. Power Sources* **2019**, 427, 194-200.
[19] Zhu, Y., Zhou, W., Zhong, Y., Bu, Y., Chen, X., Zhong, Q., Liu, M., Shao, Z. A Perovskite Nanorod as Bifunctional Electrocatalyst for Overall Water Splitting. *Adv. Energy Mater.* **2017**, 7, 1602122.
[20] Wang, J., Gao, Y., Chen, D., Liu, J., Zhang, Z., Shao, Z., Ciucci, F. Water Splitting with an Enhanced Bifunctional Double Perovskite. *ACS Catal.* **2018**, 8, 364-371.
[21] Islam, Q. A., Majee, R., Bhattacharyya, S. Bimetallic nanoparticle decorated perovskite oxide for state-of-the-art trifunctional electrocatalysis. *J. Mater. Chem. A* **2019**, 7, 19453-19464.
[22] Ji, D., Liu, C., Yao, Y., Luo, L., Wang, W., Chen, Z. Cerium substitution in $LaCoO_3$ perovskite oxide as bifunctional electrocatalysts for hydrogen and oxygen evolution reactions. *Nanoscale* **2021**, 13, 9952.
[23] Zhang, Z., Chen, Y., Dai, Z., Tang, S., Chen, D. Promoting hydrogen-evolution activity and stability of perovskite oxides via effectively lattice doping of molybdenum. *Electrochim. Acta* **2019**, 312, 128-136.
[24] Xu, X., Chen, Y., Zhou, W., Zhu, Z., Su, C., Liu, M., Shao, Z. A Perovskite Electrocatalyst for Efficient Hydrogen Evolution Reaction. *Adv. Mater.* **2016**, 28, 6442-6448.
[25] Dai, J., Zhu, Y., Zhong, Y., Miao, J., Lin, B., Zhou, W., Shao, Z. Enabling High and Stable Electrocatalytic Activity of Iron-Based Perovskite Oxides for Water Splitting by Combined Bulk Doping and Morphology Designing. *Adv. Mater. Interfaces* **2019**, 6, 1801317.
[26] Oh, N. K., Kim, C., Lee, J., Kwon, O., Choi, Y., Jung, G. Y., Lim, H. Y., Kwak, S. K., Kim, G., Park, H. In-situ local phase-transitioned $MoSe_2$ in $La_{0.5}Sr_{0.5}CoO_{3-\delta}$ heterostructure and stable overall water electrolysis over 1000 hours. *Nat. Commun.* **2019**, 10, 1723.
[27] Wang, Y., Wang, Z., Jin, C., Li, C., Li, X., Li, Y., Yang, R., Liu, M. Enhanced overall water electrolysis on a bifunctional perovskite oxide through interfacial engineering. *Electrochim. Acta* **2019**, 318, 120-129.